







In situ tuning of electronic structure of catalysts using controllable hydrogen spillover for enhanced selectivity

Mi Xiong^{1,2}, Zhe Gao ¹✉, Peng Zhao ¹, Guofu Wang¹, Wenjun Yan¹, Shuangfeng Xing^{1,2}, Pengfei Wang¹, Jingyuan Ma³, Zheng Jiang ³, Xingchen Liu ¹, Jiping Ma⁴, Jie Xu ⁴ & Yong Qin ^{1,2}✉

In situ tuning of the electronic structure of active sites is a long-standing challenge. Herein, we propose a strategy by controlling the hydrogen spillover distance to in situ tune the electronic structure. The strategy is demonstrated to be feasible with the assistance of $\text{CoO}_x/\text{Al}_2\text{O}_3/\text{Pt}$ catalysts prepared by atomic layer deposition in which CoO_x and Pt nanoparticles are separated by hollow Al_2O_3 nanotubes. The strength of hydrogen spillover from Pt to CoO_x can be precisely tailored by varying the Al_2O_3 thickness. Using $\text{CoO}_x/\text{Al}_2\text{O}_3$ catalyzed styrene epoxidation as an example, the $\text{CoO}_x/\text{Al}_2\text{O}_3/\text{Pt}$ with 7 nm Al_2O_3 layer exhibits greatly enhanced selectivity (from 74.3% to 94.8%) when H_2 is added. The enhanced selectivity is attributed to the introduction of controllable hydrogen spillover, resulting in the reduction of CoO_x during the reaction. Our method is also effective for the epoxidation of styrene derivatives. We anticipate this method is a general strategy for other reactions.

¹State Key Laboratory of Coal Conversion, Institute of Coal Chemistry, Chinese Academy of Sciences, 030001 Taiyuan, China. ²Center of Materials Science and Optoelectronics Engineering, University of Chinese Academy of Sciences, 100049 Beijing, China. ³Shanghai Synchrotron Radiation Facility, Shanghai Institute of Applied Physics, Chinese Academy of Sciences, 201204 Shanghai, China. ⁴State Key Laboratory of Catalysis, Dalian National Laboratory for Clean Energy, Dalian Institute of Chemical Physics, Chinese Academy of Sciences, 116023 Dalian, China. ✉email: gaozhe@sxicc.ac.cn; qinyong@sxicc.ac.cn

Highly efficient and selective catalysts are important for the industrial production of commodity chemicals, as well as fine chemicals and pharmaceuticals¹. The development of new heterogeneous catalysts for carrying out multipath reactions with high selectivity to achieve high-yield production of target chemicals is a longstanding challenge^{2,3}. The final product distribution, i.e., the selectivity of a reaction over a given catalyst, is determined by the relative activation barrier among different reaction paths, which in nature, primarily depend on the electronic structure of the catalytic active sites^{4–6}. However, under reaction conditions, the electronic structures of active sites are easily affected by temperature, atmosphere, and absorbed species^{7,8}. It is difficult to control the active sites to maintain the optimal electronic structure during the reaction, which favors producing more target products. Some researchers have devoted substantial effort to studying how to control and tune the electronic structures of the active sites responsible for activity and selectivity under real reaction conditions^{9,10}. In contrast to numerous studies on identifying catalytically active sites under real-time reaction conditions^{11–14}, limited methods have been reported for controlling and tuning the electronic structure of active sites during a reaction.

In general, the hydrogen migration from the metal particles to the support, i.e., hydrogen spillover, is a well-known phenomenon in heterogeneous catalysis and is involved in many important reactions^{15–24}. The efficiency and spatial extent of hydrogen spillover strongly depend on the types of supports^{25,26}. For instance, a well-defined model system demonstrated that on the nonreducible alumina support, hydrogen spillover is limited to short distances, with the hydrogen flux decreasing over distance to create a concentration gradient²⁵. In-depth understanding of hydrogen spillover can not only help to explain experimental phenomena but also aid the design of advanced catalysts with enhanced catalytic performances^{27–35}. Being inspired by these researches, we posit that there is an opportunity for an approach to modulating the electronic structure of active sites through regulating hydrogen spillover strength for enhanced catalytic performance.

In this work, using the CoO_x catalyzed epoxidation reaction of styrene as an example, we propose an approach to tune the electronic structure of cobalt species during the reaction by the introduction of controllable hydrogen spillover, to enhance the selectivity of styrene oxide (SO). To demonstrate the strategy, a $\text{CoO}_x/\text{Al}_2\text{O}_3/\text{Pt}$ catalyst is prepared by a facile and general template-assisted atomic layer deposition (ALD) method^{36–38}, in which CoO_x and Pt nanoparticles are attached on the outer and inner surfaces of Al_2O_3 nanotubes, respectively. The strength of hydrogen spillover from Pt to CoO_x can be precisely tailored by varying the thickness of the Al_2O_3 layer. The $\text{CoO}_x/\text{Al}_2\text{O}_3/\text{Pt}$ catalyst with 7 nm-thick Al_2O_3 layer exhibits greatly enhanced selectivity (from 74.3% to 94.8%) when H_2 atmosphere is introduced. Detailed analyses reveal that the cobalt species under the oxidation condition are reduced to a lower oxidation state by introducing the controllable hydrogen spillover, leading to a higher SO selectivity.

Results

Synthesis and characterization of the catalysts. $\text{CoO}_x/\gamma\text{Al}_2\text{O}_3/\text{Pt}$ catalysts with a separating Al_2O_3 layer were obtained using carbon nanocoils (CNCs) as sacrificial templates (Supplementary Fig. 1). First, Pt nanoparticles and an Al_2O_3 layer were deposited onto CNCs by Pt ALD and Al_2O_3 ALD, respectively. Subsequently, the CNC templates were removed by calcination under ambient atmosphere. Finally, CoO_x nanoparticles were deposited by CoO_x ALD, producing $\text{CoO}_x/\gamma\text{Al}_2\text{O}_3/\text{Pt}$ (where γ is the cycle

numbers of ALD Al_2O_3). For comparison, two reference catalysts ($\text{CoO}_x/50\text{Al}_2\text{O}_3$ and $50\text{Al}_2\text{O}_3/\text{Pt}$) were also synthesized by a similar method.

Figure 1a–c present the structure diagrams of $\text{CoO}_x/50\text{Al}_2\text{O}_3$, $\text{CoO}_x/50\text{Al}_2\text{O}_3/\text{Pt}$, and $\text{CoO}_x/100\text{Al}_2\text{O}_3/\text{Pt}$. Figure 1d–f show transmission electron microscopy (TEM) images of the three catalysts. TEM images of other catalysts, including $\text{CoO}_x/\gamma\text{Al}_2\text{O}_3/\text{Pt}$ with different cycles of ALD Al_2O_3 (35, 65, 80, and 300) and the reference catalyst ($50\text{Al}_2\text{O}_3/\text{Pt}$), are shown in Supplementary Fig. 2. For all TEM images, Al_2O_3 hollow structures can be clearly observed. The $\text{CoO}_x/\gamma\text{Al}_2\text{O}_3/\text{Pt}$ with different Al_2O_3 cycles (35, 50, 65, 80, 100, and 300) possess varied Al_2O_3 thicknesses from 5, 7, 9, 11, 14, to 41 nm. Regardless of Al_2O_3 thicknesses, the outer CoO_x and the inner Pt nanoparticles have similar average diameters (Supplementary Figs. 3 and 4), which is consistent with X-ray diffraction (XRD) result (Supplementary Fig. 7 and Supplementary Table 1). A high-resolution TEM (HRTEM) image of $\text{CoO}_x/50\text{Al}_2\text{O}_3/\text{Pt}$ is shown in Supplementary Fig. 5. The high-angle annular dark field scanning transmission electron microscopy (HAADF-STEM) images (Fig. 1h, i) of $\text{CoO}_x/50\text{Al}_2\text{O}_3/\text{Pt}$ and $\text{CoO}_x/100\text{Al}_2\text{O}_3/\text{Pt}$ clearly show that Pt nanoparticles are confined in Al_2O_3 nanotubes. Energy-dispersive X-ray spectroscopy (EDS) mappings of the catalysts show that the distributions of Co, O, Al, and Pt (Fig. 1j and l) are consistent with the positions of the CoO_x , Al_2O_3 , and Pt layers. Further, the distributions of Co, Al, and Pt in $\text{CoO}_x/50\text{Al}_2\text{O}_3/\text{Pt}$ were revealed clearly by STEM image and EDX mapping (Fig. 2a–d) of a cross-sectional specimen, prepared by focused ion beam (FIB) milling along the vertical direction of the Al_2O_3 nanotubes. The line-scanning profile (Fig. 2e) of cross-sectional composition shows that the signal of Co species was not detected in the Al_2O_3 nanotubes, which clearly demonstrates the separated structure of $\text{CoO}_x/50\text{Al}_2\text{O}_3/\text{Pt}$. The Al peak at ~ 4.5 nm is ascribed to signal of powder (from the FIB ion milling) remained in the space nearby the outer surface of the sample (Supplementary Fig. 6). The Co and Pt contents in the catalysts, measured by inductively coupled plasma-atomic emission spectrometry (ICP-AES), are shown in Supplementary Table 2. N_2 sorption experiments (Supplementary Fig. 8 and Supplementary Table 3) demonstrate that all the catalysts possess similar average pore diameter, while their Brunauer–Emmett–Teller (BET) surface areas and pore volumes increase with the decrease of Al_2O_3 thicknesses.

X-ray photoelectron spectroscopy (XPS) results (Fig. 3a) reveal the coexistence of Co^{3+} and Co^{2+} . Compared to the spinel Co_3O_4 , the main $2p$ peaks of $\text{CoO}_x/50\text{Al}_2\text{O}_3$, $\text{CoO}_x/50\text{Al}_2\text{O}_3/\text{Pt}$, and $\text{CoO}_x/100\text{Al}_2\text{O}_3/\text{Pt}$ shift to higher binding energy (the $2p_{3/2}$ peaks shift from 779.5 to 780.0 eV and the $2p_{1/2}$ peaks shift from 794.7 to 795.9 eV), and the satellite peaks appear (785.6 eV ($2p_{3/2}$ sat) and 802.3 eV ($2p_{1/2}$ sat)), indicating that the as-prepared CoO_x nanoparticles consist of both Co^{2+} and Co^{3+} species^{39,40}. Hydrogen temperature-programmed reduction (H_2 -TPR) was also employed (Fig. 3b). Compared to $\text{CoO}_x/50\text{Al}_2\text{O}_3$, the peak intensity of $\text{CoO}_x/50\text{Al}_2\text{O}_3/\text{Pt}$ centered at 622 °C decreases significantly, which is because the CoO_x species can be additionally reduced by the spilled active hydrogen from Pt nanoparticles. The peak intensity of $\text{CoO}_x/100\text{Al}_2\text{O}_3/\text{Pt}$ centered at 626 °C is remained, possibly because the Al_2O_3 layer of 100 ALD cycles (14 nm) is too thick and the hydrogen spillover effect is greatly weakened. The differences in reducibility of Co (Supplementary Table 4) demonstrate that the flux of spilled hydrogen species on the nonreducible Al_2O_3 support decreases with increasing distance.

Catalytic performance. The epoxidation of olefins is an important chemical reaction since epoxides are key intermediates in

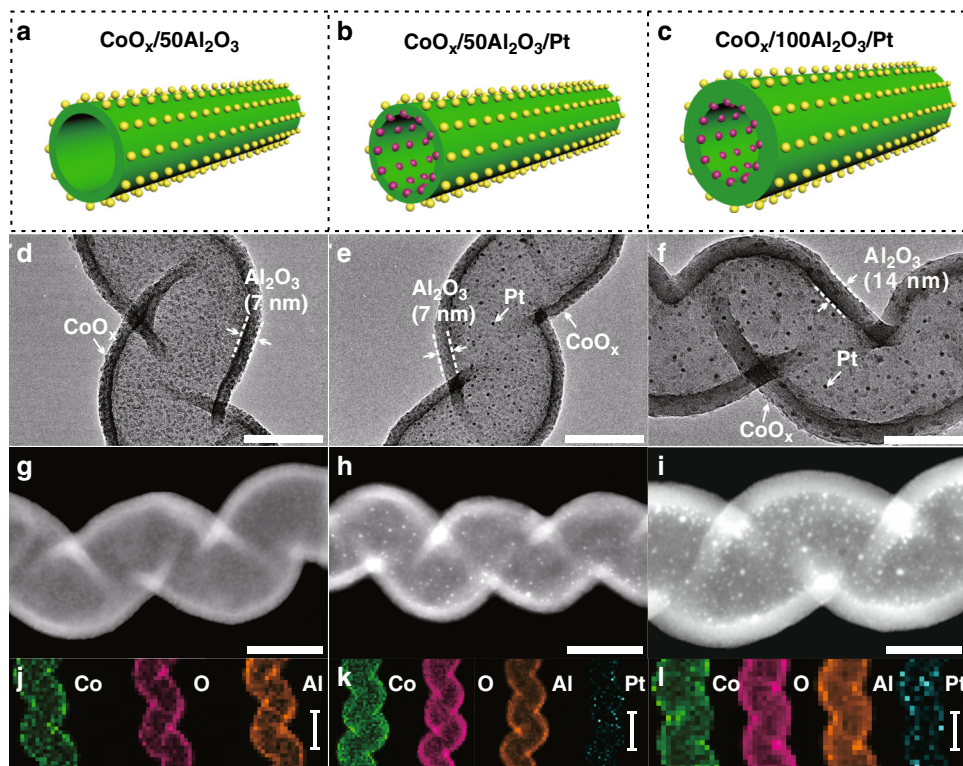


Fig. 1 Structural characterization of the catalysts. **a–c** Structure diagrams (The green tubes represent Al_2O_3 . The magenta and yellow balls represent Pt and CoO_x , respectively), **d–f** TEM images (scale bar, 50 nm), **g–i** HAADF-STEM images (scale bar, 50 nm), and **j–l** EDX elemental mappings (scale bar, 100 nm) of the catalysts. **a, d, g, j**: $\text{CoO}_x/50\text{Al}_2\text{O}_3$; **b, e, h, k**: $\text{CoO}_x/50\text{Al}_2\text{O}_3/\text{Pt}$; and **c, f, i, l**: $\text{CoO}_x/100\text{Al}_2\text{O}_3/\text{Pt}$.

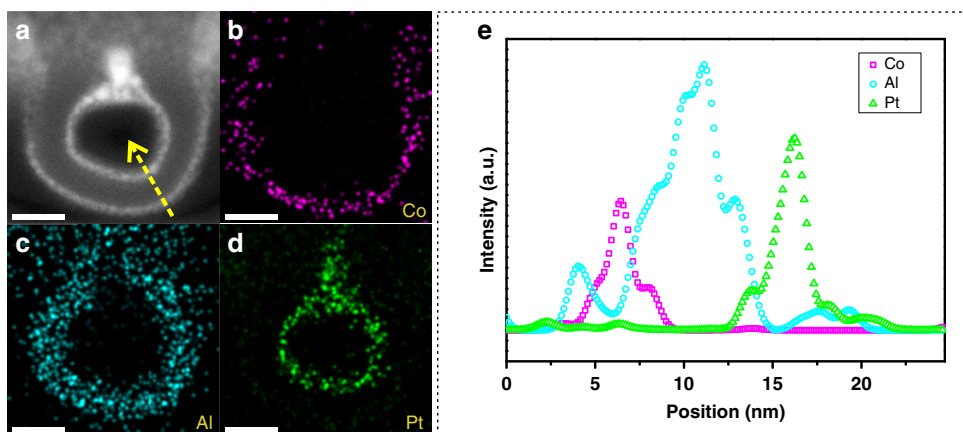


Fig. 2 Structural characterization of $\text{CoO}_x/50\text{Al}_2\text{O}_3/\text{Pt}$. **a** STEM image (scale bar, 20 nm) and **b–d** EDX elemental mappings (scale bar, 20 nm) of a cross-sectional specimen of $\text{CoO}_x/50\text{Al}_2\text{O}_3/\text{Pt}$ prepared by focused ion beam milling. **e** Compositional point profile of Co, Al, and Pt from the specimen recorded along the yellow arrow shown in **a**.

organic synthesis^{41,42}. The catalytic performances of different catalysts for the styrene epoxidation reaction with tert-butyl hydroperoxide (TBHP) as the oxidant are summarized in Table 1. Styrene was negligibly converted without a catalyst (Table 1, entry 1). For $50\text{Al}_2\text{O}_3/\text{Pt}$, only a 17.7% conversion was obtained (Table 1, entry 2). When Co-based catalysts were added, SO was formed as the major product, and benzaldehyde (BzH) was produced as a byproduct. For $\text{CoO}_x/50\text{Al}_2\text{O}_3$, the reaction can be efficiently catalyzed, with 93% conversion and 74.3% SO selectivity (Table 1, entry 3). All of the attempts, including the pre-reduction treatment (Table 1, entry 4), the increase of the ratio of TBHP/styrene (Supplementary Fig. 9), the addition of a Pt component to the catalyst (namely $\text{CoO}_x/50\text{Al}_2\text{O}_3/\text{Pt}$) (Table 1,

entry 6), and the introduction of H_2 into the reaction system (H_2 -TBHP) (Table 1, entry 5), failed to enhance the SO selectivity of $\text{CoO}_x/50\text{Al}_2\text{O}_3$. However, when H_2 was introduced into the reaction, the SO selectivity (94.8%) of $\text{CoO}_x/50\text{Al}_2\text{O}_3/\text{Pt}$ in the H_2 -TBHP condition (Table 1, entry 7) was remarkably increased by 20.5% compared to $\text{CoO}_x/50\text{Al}_2\text{O}_3$ in the TBHP condition. Although its conversion (82.5%) was slightly reduced, the decreased conversion was easily compensated by prolonging the reaction time. During the entire reaction process, the SO selectivity of the $\text{CoO}_x/50\text{Al}_2\text{O}_3/\text{Pt}$ in the H_2 -TBHP condition is greatly higher compared with that of the $\text{CoO}_x/50\text{Al}_2\text{O}_3$ in the TBHP condition under the same styrene conversion (Supplementary Fig. 10). After reaction, the distributions of the inner Pt

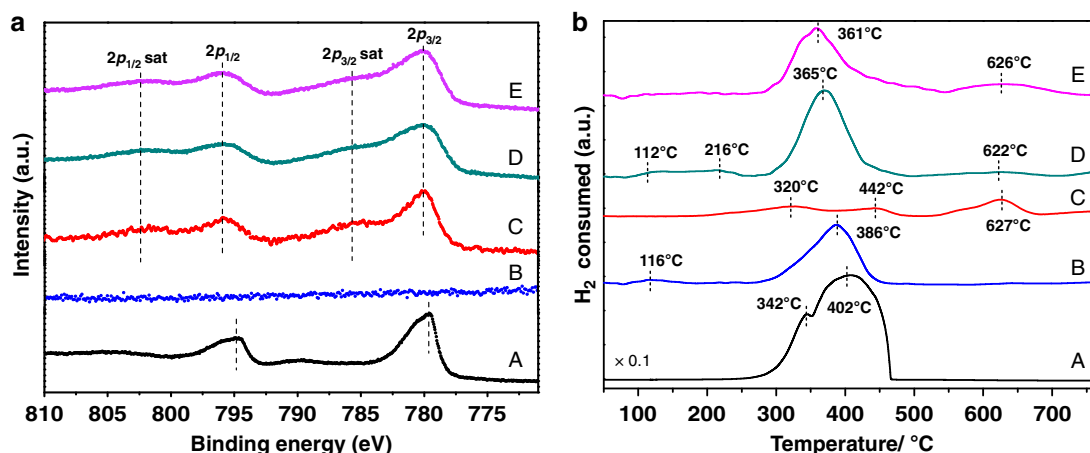


Fig. 3 Electronic structure and chemisorption characterizations. **a** XPS Co 2p analysis and **b** H₂-TPR profiles of (A) Co₃O₄ as reference, (B) 50Al₂O₃/Pt, (C) CoO_x/50Al₂O₃, (D) CoO_x/50Al₂O₃/Pt, and (E) CoO_x/100Al₂O₃/Pt.

Table 1 Catalytic performances of the catalysts for styrene epoxidation reaction in different conditions^a.

Entry	Atmosphere	Catalysts	Conversion (%)	SO sel. (%)
1	-	-	9.9	37.6
2	-	50Al ₂ O ₃ /Pt	17.7	72.4
3	-	CoO _x /50Al ₂ O ₃	93.0	74.3
4	-	Pre-reduced CoO _x /50Al ₂ O ₃ ^b	91.2	73.7
5	H ₂	CoO _x /50Al ₂ O ₃	89.8	75.9
6	-	CoO _x /50Al ₂ O ₃ /Pt	93.4	76.2
7	H ₂	CoO _x /50Al ₂ O ₃ /Pt	82.5	94.8

^aReaction conditions: 3.5 mmol styrene, 7 mmol TBHP (70% in water), 20 ml acetonitrile and catalysts with the same CoO_x content at 80 °C for 8 h.

^bReducing CoO_x/50Al₂O₃ at 350 °C for 1 h before reaction.

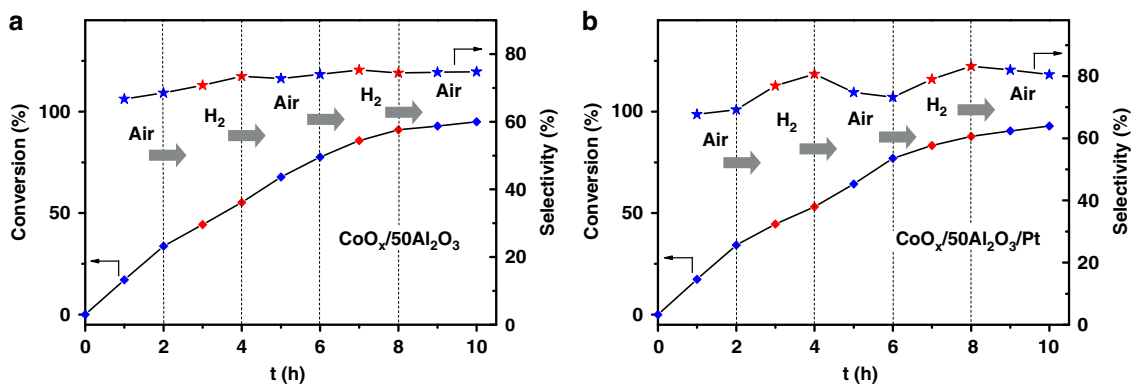


Fig. 4 H₂ pulse experiments. The evolution of styrene conversion and SO selectivity with reaction atmosphere and time over **a** CoO_x/50Al₂O₃ and **b** CoO_x/50Al₂O₃/Pt.

and the outer CoO_x nanoparticles for CoO_x/50Al₂O₃/Pt remain (Supplementary Fig. 11), and no obvious detachment of nanoparticles is observed, indicating that the catalyst is stable during the reaction.

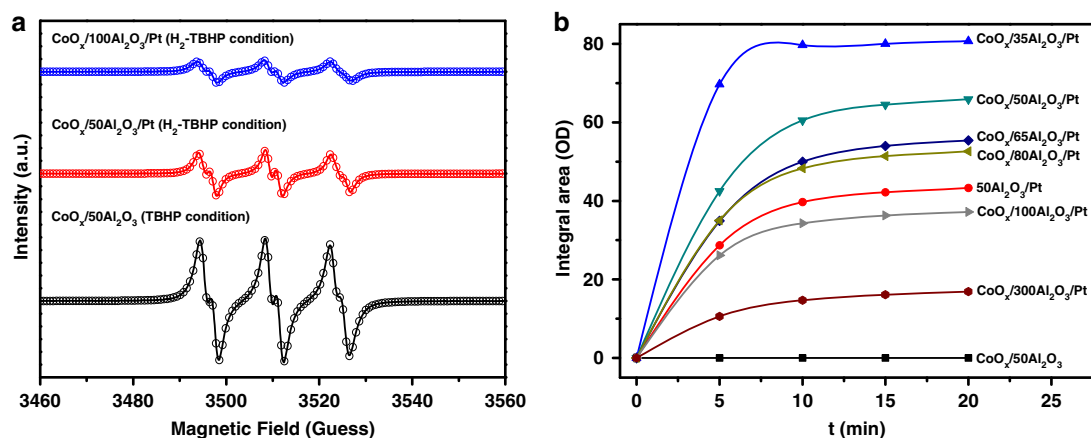
Further, H₂ pulse experiments were carried out for CoO_x/50Al₂O₃ and CoO_x/50Al₂O₃/Pt with alternating pulse of H₂ and air (Fig. 4a, b). During the reaction, for CoO_x/50Al₂O₃, the conversion and selectivity were almost unaffected by the alternate reaction atmosphere. For CoO_x/50Al₂O₃/Pt, when air was displaced by H₂, the increase of conversion slowed down and the SO selectivity was increased obviously. When H₂ was

displaced by air, the opposite phenomenon occurred. This control experiment straightforwardly indicates that the introduction of active hydrogen (Pt and H₂) plays an essential role in enhancing the selectivity of the catalysts for styrene epoxidation reaction.

The effect of the distance between CoO_x and Pt components corresponding to the thicknesses of the Al₂O₃ layer on the catalytic performance has been investigated (Table 2 and Supplementary Table 5). The thicknesses of the Al₂O₃ layer are precisely regulated by varying the cycle numbers of ALD Al₂O₃. In TBHP condition, the catalytic performances of CoO_x/γAl₂O₃/Pt

Table 2 Catalytic performances of the catalysts with different Al₂O₃ cycles for styrene epoxidation reaction.

Entry	Catalysts	Distance (nm)	TBHP condition		H ₂ -TBHP condition	
			Conversion (%)	SO sel. (%)	Conversion (%)	SO sel. (%)
1	CoO _x /35Al ₂ O ₃ /Pt	5	91.0	77.5	83.5	93.9
2	CoO _x /50Al ₂ O ₃ /Pt	7	93.4	76.2	82.5	94.8
3	CoO _x /65Al ₂ O ₃ /Pt	9	92.5	78.2	85.6	86.5
4	CoO _x /80Al ₂ O ₃ /Pt	11	93.0	76.4	89.0	77.1
5	CoO _x /100Al ₂ O ₃ /Pt	14	92.0	76.3	90.2	76.8
6	CoO _x /300Al ₂ O ₃ /Pt	41	94.8	74.8	91.9	75.1

**Fig. 5** Catalytic mechanism analyses. **a** Experimental EPR spectra (lines) and simulated spectra (open circles) for a mixture of PBN-OOC(CH₃)₃ and PBN-OC(CH₃)₃. **b** Intensity of the $\nu(\text{OD})$ band during exposure of samples in (D₂:H₂ = 1:1) at a total D₂/H₂ flow rate of 30 ml min⁻¹ at 80 °C and 1 atm.

are similar. However, when H₂ was introduced, their catalytic performances exhibited obvious differences. Varying the cycle numbers of ALD Al₂O₃ from 35 to 65, the activities of the three catalysts in the H₂-TBHP condition decreased compared with those of the corresponding catalysts in the TBHP condition, whereas the SO selectivities show obvious improvements with the highest value of 94.8% for CoO_x/50Al₂O₃/Pt (Table 2, entries 1–3). With a further increase of cycle numbers (over 80), the activities and SO selectivities of CoO_x/80Al₂O₃/Pt, CoO_x/100Al₂O₃/Pt, and CoO_x/300Al₂O₃/Pt in the H₂-TBHP condition are similar to that of the corresponding catalysts in the TBHP condition (Table 2, entries 4–6). At low conversions, CoO_x/50Al₂O₃/Pt catalyst also exhibits the greatest improvement of SO selectivity among these catalysts (Supplementary Fig. 12). Therefore, it can be seen that a precisely controlled CoO_x-Pt distance is critically important for the remarkably enhanced SO selectivity.

Catalytic mechanism. To uncover the potential mechanism for the enhanced SO selectivity, a series of experiments and characterizations were carried out. Isotope-labeling experiments were conducted to track the transfer pathways of split hydrogen species. For CoO_x/50Al₂O₃/Pt in the D₂-TBHP condition, the deuterium signal was not found in the mass spectrometry results of BzH and SO (Supplementary Fig. 13), demonstrating that the active hydrogen species were not directly involved in the oxidation of organic substrates.

A free radical scavenger (butylated hydroxytoluene, BHT) was added to the reaction to further study the reaction mechanism. For CoO_x/50Al₂O₃ in the TBHP condition, and CoO_x/50Al₂O₃/Pt and CoO_x/100Al₂O₃/Pt in the H₂-TBHP condition, the conversion of styrene stopped after the addition of BHT (Supplementary

Fig. 14), indicating that the radical pathway has an important contribution to the reaction mechanism. Moreover, according to the electron paramagnetic resonance (EPR) results (Fig. 5a, Supplementary Fig. 15, and Supplementary Table 6), two kinds of radicals, i.e., tert-butylperoxy and tert-butyloxy radicals (tBuOO· and tBuO·), can be detected in the three cases. These results indicate that the styrene epoxidation reaction over Co-based catalysts experienced a radical process, and the kinds of the radicals were the same in the three cases.

The existence of hydrogen spillover from Pt to CoO_x through the nonreducible Al₂O₃ support was confirmed by H-D exchange experiments (Fig. 5b and Supplementary Fig. 16). Figure 5b shows the H-D exchange rates of CoO_x/50Al₂O₃, 50Al₂O₃/Pt, and CoO_x/ γ Al₂O₃/Pt (γ = 35, 50, 65, 80, 100, and 300), indicating that the flux of spilled deuterium species from Pt to CoO_x on the nonreducible Al₂O₃ support decreases with increasing distance. The hydrogen spillover was also confirmed by the color change in the mixture of the catalyst and WO₃ nanowires (Supplementary Fig. 17). There are debates on the existence of hydrogen spillover on nonreducible support (SiO₂, Al₂O₃, and zeolite). It was argued that hydrogen spillover to defect-free surfaces of nonreducible metal oxides cannot take place, but spillover to a non-reducible support with defects is possible¹⁶. In recent years, more and more evidence demonstrates that although Al₂O₃ is a non-reducible oxide, hydrogen spillover can occur on it^{25,43–49}. In this work, the obtained Al₂O₃ is amorphous (Supplementary Fig. 7) and thus many defects exist. The nonreducible Al₂O₃ support was calcined at high temperature, which may result in the formation of a small amount of micropores⁵⁰. Thus, the active hydrogen species may spill over the surface of the micropores or through the defects of Al₂O₃ layer.

To reveal the electronic structures of cobalt species, X-ray absorption fine structure (XAFS) of the catalysts was investigated

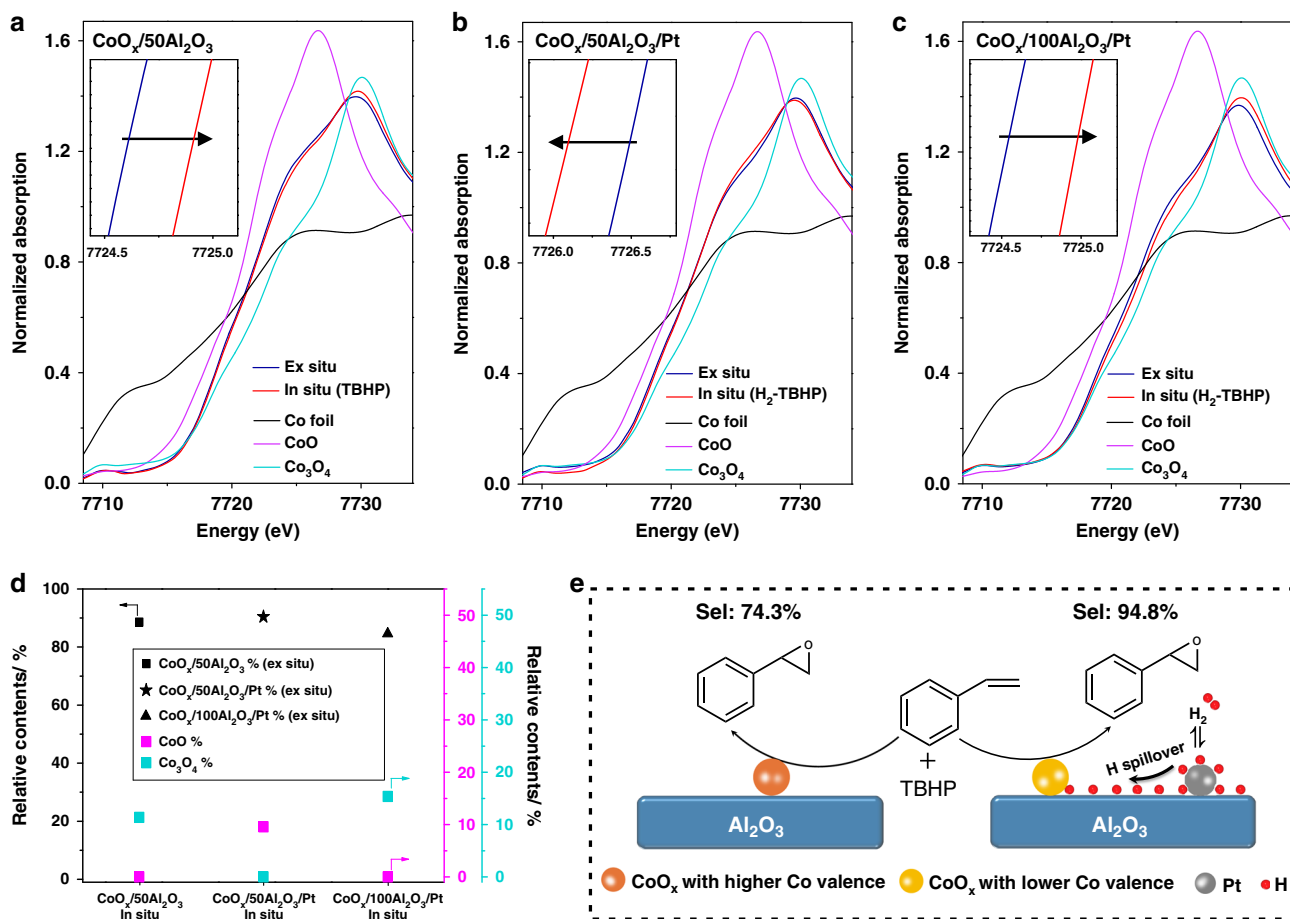


Fig. 6 XANES spectra of the catalysts and proposed mechanisms. **a–c** Ex situ and in situ Co K-edge XANES spectra of $\text{CoO}_x/50\text{Al}_2\text{O}_3$, $\text{CoO}_x/50\text{Al}_2\text{O}_3/\text{Pt}$, and $\text{CoO}_x/100\text{Al}_2\text{O}_3/\text{Pt}$, and spectra of reference samples (Co foil, CoO, and Co_3O_4). Insets show the expanded sections of absorption edges. **d** The results of the linear combination fitting for the in situ spectra of the catalysts. For each catalyst, the in-situ spectrum is fitted by a linear combination of the ex-situ spectrum and the spectra of reference samples (Co_3O_4 and CoO). **e** Proposed reaction mechanisms for $\text{CoO}_x/50\text{Al}_2\text{O}_3$ in the TBHP condition and $\text{CoO}_x/50\text{Al}_2\text{O}_3/\text{Pt}$ in the H_2 -TBHP condition. In the presence of controllable hydrogen spillover, cobalt species with a lower valence state are beneficial to the enhanced selectivity.

(Fig. 6a–c). The ex situ X-ray absorption near-edge structure (XANES) profiles show that the positions of the white line peaks for the $\text{CoO}_x/50\text{Al}_2\text{O}_3$, $\text{CoO}_x/50\text{Al}_2\text{O}_3/\text{Pt}$, and $\text{CoO}_x/100\text{Al}_2\text{O}_3/\text{Pt}$ are all located between the peaks of the rock-salt CoO and spinel Co_3O_4 , indicating that the oxidation states of cobalt species for as-prepared catalysts include both Co^{3+} and Co^{2+} , which is consistent with the XPS result. In the presence of TBHP, compared with the ex situ spectrum, the absorption edge of the in-situ spectrum for $\text{CoO}_x/50\text{Al}_2\text{O}_3$ shifted to higher energy (Fig. 6a), revealing that the cobalt species in the reaction is at a higher oxidation state. The changes in the valence of catalyst are not significant, because of the mild reaction conditions (80°C and atmosphere pressure). When H_2 was introduced into the reaction system, no obvious difference was observed in the H_2 -TBHP condition compared with in the TBHP condition for $\text{CoO}_x/50\text{Al}_2\text{O}_3$ (Supplementary Fig. 18). For $\text{CoO}_x/100\text{Al}_2\text{O}_3/\text{Pt}$, a distinct increase in the cobalt oxidation state was also observed in the reaction (H_2 -TBHP condition) (Fig. 6c). However, for $\text{CoO}_x/50\text{Al}_2\text{O}_3/\text{Pt}$, the absorption edge of the in-situ spectrum shifted to lower energy (Fig. 6b), meaning a decrease in the cobalt oxidation state in the H_2 -TBHP condition. To quantitatively reveal the change in the cobalt oxidation states during the reaction, the in-situ XANES spectrum is simulated by a linear combination of the ex-situ spectrum of the as-prepared catalyst and the spectra of reference samples (Co_3O_4 and CoO) (Supplementary Fig. 19 and

Supplementary Table 7). For $\text{CoO}_x/50\text{Al}_2\text{O}_3$ in the TBHP condition and $\text{CoO}_x/100\text{Al}_2\text{O}_3/\text{Pt}$ in the H_2 -TBHP condition, extra Co_3O_4 (11.4% and 15.4%, respectively) is formed, as shown in Fig. 6d. However, for $\text{CoO}_x/50\text{Al}_2\text{O}_3/\text{Pt}$ in the H_2 -TBHP condition, extra CoO (9.6%) is formed. The k^2 -weighted Fourier-transformed extended X-ray absorption fine structure (FT-EXAFS) spectra (Supplementary Fig. 20) and their curve fitting results (Supplementary Table 8) are consistent with the conclusions drawn from the XANES experiments.

Discussion

Our results show that epoxidation selectivity can be obviously enhanced after controllable hydrogen spillover was introduced. The possible reasons of the enhanced selectivity were revealed by detailed experiments and characterizations.

After Pt and H_2 were introduced into the epoxidation reaction, the CoO_x catalyzed epoxidation reaction still experienced a radical process and the kinds of radicals were the same, which can be concluded from the radical scavenging and EPR results. On the other hand, for $\text{CoO}_x/\gamma\text{Al}_2\text{O}_3/\text{Pt}$, they are similar in sizes of nanoparticles (TEM and XRD) and pore diameter (N_2 sorption) regardless of the thicknesses of Al_2O_3 . Their catalytic performances are similar in TBHP condition. Moreover, the pre-reduction treatment of $\text{CoO}_x/50\text{Al}_2\text{O}_3$ further indicates the

enhanced selectivity is not ascribed to the ex-situ oxidation states of fresh catalysts.

In contrast, when H₂ was introduced into the reaction, the catalytic performances of the CoO_x/γAl₂O₃/Pt with different Al₂O₃ thicknesses exhibited obvious differences. The color change of WO₃ nanowires and H–D exchange experiments suggest that when H₂ was introduced into the reaction system, hydrogen spillover can occur and the strength of hydrogen spillover decreases with increasing distance, which is in good accordance with the TPR result. Moreover, isotope-labeling experiments demonstrate that the active hydrogen species are not directly involved in the oxidation of organic substrates. For the catalyst with enhanced selectivity, the CoO_x–Pt distance (several nanometers) is comparable to the distance of hydrogen spillover on Al₂O₃, implying that the controllable hydrogen spillover is responsible for the enhanced selectivity. The in situ XAFS results further confirm the explanation. It clearly reveals that the electronic structures of cobalt species during the epoxidation reaction can be successfully modulated through controlling the hydrogen spillover distance. For CoO_x/50Al₂O₃/Pt in H₂-TBHP condition, the cobalt species are reduced to a lower oxidation state, while for CoO_x/50Al₂O₃ in TBHP condition and CoO_x/100Al₂O₃/Pt in H₂-TBHP condition, the cobalt species are oxidized to a higher oxidation state. For the epoxidation reaction, one common understanding of the reaction mechanism is recognized that catalysts affect the reactions by bonding of oxygen to the metal^{51–54}. The electronic structure of catalyst at reaction conditions affects the strength of the Co–O bond in the catalyst, which further determines the selectivity of epoxides.

In addition to hydrogen spillover on the Al₂O₃ support, other possible migration mechanisms of active hydrogen species, including carbon impurities and water-assisted H shuttling, are also considered. Carbon impurities are proposed as an alternative hydrogen migration path on nonreducible support¹⁶. Water-assisted H shuttling can accelerate proton transfer and is proposed to explain the enhanced performance observed in the presence of water for hydrogenation reactions^{55,56}. However, the distance of hydrogen spillover on carbon species is far beyond the range of several nanometers^{11,24}. Similarly, hydrogen shuttling is a remote promotional effect⁵⁷. These mechanisms cannot fit our catalytic results well.

Based on all above results, it can be concluded that the enhanced selectivity is attributed to the introduction of controllable hydrogen spillover, which is further confirmed by the H₂ pulse experiments. In the presence of controllable hydrogen spillover, cobalt species with a lower valence state are more beneficial for enhanced catalytic selectivity, as shown in Fig. 6. Based on the successful demonstration of in-situ tailoring of Co valence by hydrogen spillover, we can expect that the selectivity

can also be changed over a CoO_xPt/50Al₂O₃ catalyst with the closely contacted Pt and CoO_x (Supplementary Fig. 21) due to the effect of hydrogen spillover. As expected, the SO selectivity of CoO_xPt/50Al₂O₃ in the H₂-TBHP condition is also increased compared to that in the TBHP condition (Supplementary Table 9). This further confirms that the introduction of controllable hydrogen spillover is responsible for the enhanced selectivity.

The strategy by introducing controllable hydrogen spillover into reaction was also successfully applied to the epoxidation of a variety of styrene derivatives (Table 3). In all cases, CoO_x/50Al₂O₃/Pt exhibits greatly enhanced selectivities (up to over 90%) via the introduction of controllable hydrogen spillover. Further, the Pt/50Al₂O₃/CoO_x (Supplementary Fig. 22), which was produced by exchanging the deposition sequences of Pt and CoO_x nanoparticles, also exhibits enhanced SO selectivity through the introduction of controllable hydrogen spillover (Supplementary Table 10). In addition to cobalt catalysts, iron catalysts were also applied for styrene epoxidation. The SO selectivity of FeO_x/50Al₂O₃/Pt in the H₂-TBHP condition is higher than that of FeO_x/50Al₂O₃ in the TBHP condition (Supplementary Fig. 23). These results demonstrate that the introduction of controllable hydrogen spillover for enhanced selectivity is a general method.

In summary, we have demonstrated a strategy, involving the introduction of controllable hydrogen spillover to the styrene epoxidation reaction to in situ tune the electronic structure of cobalt species for enhanced SO selectivity. The strength of hydrogen spillover from Pt nanoparticles to CoO_x was tuned by altering the thickness (ALD cycles) of the separating Al₂O₃ layer. When the thickness of the Al₂O₃ layer was 7 nm, the catalyst (CoO_x/50Al₂O₃/Pt) in the H₂-TBHP condition exhibited significantly enhanced SO selectivity (over 20%) compared with the CoO_x/50Al₂O₃ catalyst in the TBHP condition. Our method of in situ electronic structure regulation, achieved through controllable hydrogen spillover, can be used for other catalytic reactions.

Methods

Synthesis of 50Al₂O₃/Pt catalysts. The synthesis of CNCs and the ALD process can be found in the Supplementary Methods. CNCs were firstly deposited with Pt nanoparticles (20 cycles) and then coated with an Al₂O₃ layer (50 cycles) by ALD, producing 50Al₂O₃/Pt/CNCs. The 50Al₂O₃/Pt/CNCs were calcinated at 500 °C for 1 h in air to remove the CNC templates, obtaining 50Al₂O₃/Pt catalysts.

Synthesis of CoO_x/50Al₂O₃ catalysts. CNCs were firstly coated with an Al₂O₃ layer (50 cycles) by ALD producing Al₂O₃/CNCs, which were calcinated at 500 °C for 1 h in air. Then the obtained hollow Al₂O₃ nanotubes were deposited with CoO_x nanoparticles (35 cycles) by ALD, obtaining CoO_x/50Al₂O₃ catalysts.

Table 3 Catalytic epoxidation of styrene derivatives in different conditions^a.

Catalysts	Condition	Substrates	t (h)	Conversion (%)	Epoxide sel. (%)
CoO _x /50Al ₂ O ₃	TBHP	<i>p</i> -methylstyrene	12	97.1	88.4
		<i>p</i> -methoxy-styrene	12	80.5	78.2
		<i>m</i> -nitrostyrene	16	68.4	68.2
		<i>m</i> -chlorostyrene	12	88.7	69.9
		2-vinyl naphthalene	12	82.1	79.8
CoO _x /50Al ₂ O ₃ /Pt	H ₂ -TBHP	<i>p</i> -methylstyrene	12	86.2	98.2
		<i>p</i> -methoxy-styrene	12	68.1	94.3
		<i>m</i> -nitrostyrene	16	59.2	92.3
		<i>m</i> -chlorostyrene	12	81.1	89.4
		2-vinyl naphthalene	12	71.5	91.5

^aReaction conditions: 3.5 mmol substrates, 7 mmol TBHP (70% in water), 20 ml acetonitrile, and catalysts with the same CoO_x content at 80 °C.

Synthesis of CoO_x/γ-Al₂O₃/Pt catalysts. CNCs were firstly deposited with Pt nanoparticles and then coated with an Al₂O₃ layer (γ = 35, 50, 65, 80, 100, 300) by ALD. After Al₂O₃ deposition, CNCs were completely enclosed by compact ALD Al₂O₃. The obtained samples were calcinated at 500 °C for 1 h in air and subsequently coated with CoO_x nanoparticles (35 cycles) by ALD, obtaining CoO_x/γ-Al₂O₃/Pt.

Synthesis of CoO_xPt/50Al₂O₃ catalysts. The hollow Al₂O₃ nanotubes prepared by the above method were deposited with Pt (20 cycles) and CoO_x nanoparticles (35 cycles) by ALD, obtaining CoO_xPt/50Al₂O₃ catalysts.

Synthesis of Pt/50Al₂O₃/CoO_x catalysts. CNCs were firstly deposited with CoO_x nanoparticles (35 cycles) and then coated with an Al₂O₃ layer (50 cycles) by ALD. The obtained samples were calcinated at 500 °C for 1 h in air and subsequently coated with Pt nanoparticles (20 cycles) by ALD, obtaining Pt/50Al₂O₃/CoO_x.

Synthesis of FeO_x/50Al₂O₃ and FeO_x/50Al₂O₃/Pt catalysts. The hollow Al₂O₃ nanotubes and the 50Al₂O₃/Pt catalysts prepared by the above method were deposited with FeO_x nanoparticles (70 cycles) by ALD, obtaining FeO_x/50Al₂O₃ and FeO_x/50Al₂O₃/Pt catalysts, respectively.

Catalyst characterizations. FIB based on high-brightness Ga liquid-metal ion sources was recorded in FIB-SEM instrument (LYRA3 XMH, TESCAN). Typically, CNCs were first dispersed on a Si substrate and then were deposited by Pt and Al₂O₃ ALD. After calcination, the CoO_x was deposited. Then the Si substrate with the CoO_x/50Al₂O₃/Pt sample was transferred into the FIB-SEM system. The sample was first protected by a carbon layer. After that, a selected part of the protected CoO_x/50Al₂O₃/Pt was lifted out of the Si substrate by FIB milling using Ga ion beam and then mounted on a TEM grid. Finally, the sample was sliced down to ~100 nm along the vertical direction of the Al₂O₃ nanotubes by the Ga ion beam for TEM analysis. The EPR spectrums of the reaction solutions were recorded on a Bruker EMX spectrometer (EMXplus-10/12) using the following settings: frequency 9.862 GHz, sweep width 3460.0 G, time constant 60 ms, modulation frequency 100 kHz, modulation width 0.5 G, microwave power 5 mW. The spin trap N-tert-butyl-α-phenylnitron (PBN) was added into the reaction solutions to form radical adducts (1:1 molar ratio between the spin trap and TBHP). The solutions were filtered and the spectra were obtained at room temperature (298 K), using capillary tubes with the same dimensions as those used for the recording of the spectra of the catalysts. H-D exchange was characterized by in-situ infrared (IR) spectroscopy. IR spectra were recorded with a Bruker IFS 66v/S spectrometer with a resolution of 2 cm⁻¹, and each spectrum is an average of 64 scans. The sample for IR spectroscopy was loaded into a diffuse reflectance infrared Fourier transform spectroscopy (DRIFTS) cell (Harrick Scientific Products, Praying Mantis™). The cell was connected to a flow system that allows recording of spectra while gases pass through and around the sample. The samples in IR cell were pretreated at 473 K for 1 h and then cooled down to 353 K in flowing He (30 mL min⁻¹). After the treatment, the samples were exposed to flowing gas (H₂ at 30 mL min⁻¹) at 353 K for 1 h, and then switched to flowing gas mixtures (H₂ at 15 mL min⁻¹, D₂ at 15 mL min⁻¹) at 353 K. The spectra of H-D exchange were recorded. The ex situ and in situ XAFS were obtained on the 1W1B beamline of the Beijing Synchrotron Radiation Facility (BSRF), Institute of High Energy Physics, Chinese Academy of Sciences, and the BL14W1 beamline of the Shanghai Synchrotron Radiation Facility (SSRF), Shanghai Institute of Applied Physics, Chinese Academy of Sciences. A Si (111) double-crystal monochromator was used to reduce the harmonic component of the monochrome beam. Co foil, CoO, and Co₃O₄ were used as reference samples and measured in transmission mode. IFEFFIT software was used to calibrate the energy scale, to correct the background signal and to normalize the intensity. The theoretical paths for Co-O and Co-Co species used for fitting three coordination shells of the experimental data were generated using the FEFF7 program. The coordination number, bond distance, Debye-Waller factor, and inner potential correction were used as variable parameters for the fitting procedures. The in-situ XANES spectrum was simulated by a linear combination of the ex-situ spectrum of the as-prepared catalyst and the spectra of reference samples (Co₃O₄ and CoO). The following formula was used: (in situ XANES) = f₁·(ex situ XANES) + f₂·(XANES of Co₃O₄) + f₃·(XANES of CoO), where f₁, f₂, and f₃ are the fractions of the as-prepared catalyst, Co₃O₄ and CoO, respectively.

The other characterizations are provided in the Supplementary Methods.

Catalytic activity measurements. Styrene epoxidation reactions over the catalysts were carried out in a 50 ml three-necked round bottom flask equipped with a magnetic stirrer in an oil bath. A mixture of catalysts with the same CoO_x content, 20 ml acetonitrile, 3.5 mmol styrene, and 7 mmol TBHP (70% TBHP in water) was introduced into the reaction vessel. Then, the reaction mixture was magnetically stirred and heated to 80 °C at atmospheric pressure. When H₂ was introduced into the reaction, the vessel was purged with purified hydrogen to remove the air at

atmospheric pressure, and then was completely sealed with rubber plugs. Heating the reaction system to 80 °C, styrene was injected through needle tube. After reaction for 8 h, the reaction mixture was separated and the liquid products collected were analyzed by gas chromatography-mass spectrometry (GC-MS, Agilent Technologies 7890A-5795C) with a capillary column (HP-5, 30 m × 25 mm × 0.25 μm). Free radical capture experiments were carried out by adding 2 mmol quenchers (BHT) into the reaction system after 1 h reaction. H₂ pulse experiments were carried out in a 50 ml three-necked round bottom flask with alternating pulse of H₂ and air. When the reaction atmosphere was displaced, the heating was stopped and each displaced process was maintained for 10 min with the gas flow rate of 30 sccm. Note that before each pulse, air or H₂ was purged by inert gas nitrogen to ensure the safety. After displacement, the vessel was completely sealed and continued to be heated. The samples were collected every hour, and the reaction atmosphere was displaced every 2 h.

Safety notices

Mixing hydrogen with an oxidant, in principle, may be not safe. In this paper, the risks are very minor considering mild reaction condition (low reaction temperature, atmospheric pressure, a small amount of H₂ (30 ml), and a round bottom flask sealed with rubber plugs). If readers attempt to repeat it, please refer to the detailed experiment process in the section of "Catalytic activity measurements".

Data availability

The data that support the findings of this study are available from the corresponding author under reasonable request.

Received: 4 February 2020; Accepted: 25 August 2020;

Published online: 22 September 2020

References

- Noyori, R. Synthesizing our future. *Nat. Chem.* **1**, 5–6 (2009).
- Somorjai, G. A. & Rioux, R. M. High technology catalysts towards 100% selectivity: fabrication, characterization and reaction studies. *Catal. Today* **100**, 201–215 (2005).
- Peng, X. et al. Impact of hydrogenolysis on the selectivity of the Fischer-Tropsch synthesis: diesel fuel production over mesoporous zeolite-Y-supported cobalt nanoparticles. *Angew. Chem. Int. Ed. Engl.* **54**, 4553–4556 (2015).
- Corma, A., Serna, P., Concepcion, P. & Calvino, J. J. Transforming nonselective into chemoselective metal catalysts for the hydrogenation of substituted nitroaromatics. *J. Am. Chem. Soc.* **130**, 8748–8753 (2008).
- Marshall, S. T. et al. Controlled selectivity for palladium catalysts using self-assembled monolayers. *Nat. Mater.* **9**, 853–858 (2010).
- Zhai, P. et al. Highly tunable selectivity for syngas-derived alkenes over zinc and sodium-modulated Fe₃C₂ catalyst. *Angew. Chem. Int. Ed. Engl.* **55**, 9902–9907 (2016).
- Weckhuysen, B. M. Determining the active site in a catalytic process: Operando spectroscopy is more than a buzzword. *Phys. Chem. Chem. Phys.* **5**, 4351–4360 (2003).
- Tanabe, T. et al. Operando X-ray absorption spectroscopy study of Pt/γ-Al₂O₃ during the total oxidation of C₃H₆. *Top. Catal.* **52**, 1433–1439 (2009).
- Zhou, Y. et al. Dopant-induced electron localization drives CO₂ reduction to C₂ hydrocarbons. *Nat. Chem.* **10**, 974–980 (2018).
- Greiner, M. T. et al. Free-atom-like d states in single-atom alloy catalysts. *Nat. Chem.* **10**, 1008–1015 (2018).
- Briggs, N. M. et al. Identification of active sites on supported metal catalysts with carbon nanotube hydrogen highways. *Nat. Commun.* **9**, 3827 (2018).
- Yang, H. et al. A highly stable copper-based catalyst for clarifying the catalytic roles of Cu⁰ and Cu⁺ species in methanol dehydrogenation. *Angew. Chem. Int. Ed. Engl.* **57**, 1836–1840 (2018).
- Wen, G., Wu, S., Li, B., Dai, C. & Su, D. S. Active sites and mechanisms for direct oxidation of benzene to phenol over carbon catalysts. *Angew. Chem. Int. Ed. Engl.* **54**, 4105–4109 (2015).
- Yang, Y. et al. In situ X-ray absorption spectroscopy of a synergistic Co-Mn oxide catalyst for the oxygen reduction reaction. *J. Am. Chem. Soc.* **141**, 1463–1466 (2019).
- Conner, W. C. & Falconer, J. L. Spillover in heterogeneous catalysis. *Chem. Rev.* **95**, 759–788 (1995).
- Prins, R. Hydrogen spillover. Facts and fiction. *Chem. Rev.* **112**, 2714–2738 (2012).
- Zhang, J. et al. Origin of synergistic effects in bicomponent cobalt oxide-platinum catalysts for selective hydrogenation reaction. *Nat. Commun.* **10**, 4166 (2019).

18. Ali, L. I., Ali, A. G. A., Aboul-Fotouh, S. M. & Aboul-Gheit, A. K. Dehydrogenation of cyclohexane on catalysts containing noble metals and their combinations with platinum on alumina support. *Appl. Catal. A* **177**, 99–110 (1999).
19. Zhang, A., Nakamura, I., Aimoto, K. & Fujimoto, K. Isomerization of n-pentane and other light hydrocarbons on hybrid catalyst. Effect of hydrogen spillover. *Ind. Eng. Chem. Res.* **34**, 1074–1080 (1995).
20. Wang, H. et al. Platinum-modulated cobalt nanocatalysts for low-temperature aqueous-phase Fischer–Tropsch synthesis. *J. Am. Chem. Soc.* **135**, 4149–4158 (2013).
21. Yang, G. et al. Design and modification of zeolite capsule catalyst, a confined reaction field, and its application in one-step isoparaffin synthesis from syngas. *Energy Fuels* **22**, 1463–1468 (2008).
22. Park, J. et al. Investigation of support effect in atomically dispersed Pt on WO_{3-x} for high utilization of Pt in hydrogen evolution reaction. *Angew. Chem. Int. Ed. Engl.* **58**, 16038–16042 (2019).
23. Yao, Y. & Goodman, D. W. Direct evidence of hydrogen spillover from Ni to Cu on Ni–Cu bimetallic catalysts. *J. Mol. Catal. A: Chem.* **383**, 239–242 (2014).
24. Phaahlamohla, T. N. et al. Effects of Co and Ru intimacy in Fischer–Tropsch catalysts using hollow carbon sphere supports: assessment of the hydrogen spillover processes. *ACS Catal.* **7**, 1568–1578 (2017).
25. Karim, W. et al. Catalyst support effects on hydrogen spillover. *Nature* **541**, 68–71 (2017).
26. Zhan, G. & Zeng, H. C. Hydrogen spillover through Matryoshka-type (ZIFs@ n -ZIFs) nanocubes. *Nat. Commun.* **9**, 3778 (2018).
27. Nabaho, D., Niemantsverdriet, J. W., Claeys, M. & van Steen, E. Hydrogen spillover in the Fischer–Tropsch synthesis: an analysis of platinum as a promoter for cobalt–alumina catalysts. *Catal. Today* **261**, 17–27 (2016).
28. Beaumont, S. K. et al. Combining in Situ NEXAFS spectroscopy and CO_2 methanation kinetics to study Pt and Co nanoparticle catalysts reveals key insights into the role of platinum in promoted cobalt catalysis. *J. Am. Chem. Soc.* **136**, 9898–9901 (2014).
29. Aitbekova, A. et al. Engineering of ruthenium-iron oxide colloidal heterostructures: improved yields in CO_2 hydrogenation to hydrocarbons. *Angew. Chem. Int. Ed. Engl.* **58**, 17451–17457 (2019).
30. Witton, T. et al. Enhanced activity, selectivity and stability of a CuO–ZnO–ZrO₂ catalyst by adding graphene oxide for CO_2 hydrogenation to methanol. *Chem. Eng. J.* **334**, 1781–1791 (2018).
31. Kyriakou, G. et al. Isolated metal atom geometries as a strategy for selective heterogeneous hydrogenations. *Science* **335**, 1209–1212 (2012).
32. Wrasman, C. J. et al. Synthesis of colloidal Pd/Au dilute alloy nanocrystals and their potential for selective catalytic oxidations. *J. Am. Chem. Soc.* **140**, 12930–12939 (2018).
33. Wang, S. et al. Activation and spillover of hydrogen on sub-1 nm palladium nanoclusters confined within sodalite zeolite for the semi-hydrogenation of alkynes. *Angew. Chem. Int. Ed. Engl.* **58**, 7668–7672 (2019).
34. Yook, S., Shin, H., Kim, H. & Choi, M. Selective dissociation of dihydrogen over dioxygen on a hindered platinum surface for the direct synthesis of hydrogen peroxide. *ChemCatChem* **6**, 2836–2842 (2014).
35. Taniya, K., Jinno, H., Kishida, M., Ichihashi, Y. & Nishiyama, S. Preparation of Sn-modified silica-coated Pt catalysts: a new PtSn bimetallic model catalyst for selective hydrogenation of crotonaldehyde. *J. Catal.* **288**, 84–91 (2012).
36. George, S. M. Atomic layer deposition: an overview. *Chem. Rev.* **110**, 111–131 (2010).
37. Gao, Z. & Qin, Y. Design and properties of confined nanocatalysts by atomic layer deposition. *Acc. Chem. Res.* **50**, 2309–2316 (2017).
38. Gao, Z. et al. Multiply confined nickel nanocatalysts produced by atomic layer deposition for hydrogenation reactions. *Angew. Chem. Int. Ed. Engl.* **54**, 9006–9010 (2015).
39. Biesinger, M. C. et al. Resolving surface chemical states in XPS analysis of first row transition metals, oxides and hydroxides: Cr, Mn, Fe, Co and Ni. *Appl. Surf. Sci.* **257**, 2717–2730 (2011).
40. Vaz, C. A. F., Prabhakaran, D., Altman, E. I. & Henrich, V. E. Experimental study of the interfacial cobalt oxide in $\text{Co}_3\text{O}_4/\alpha\text{-Al}_2\text{O}_3$ (0001) epitaxial films. *Phys. Rev. B* **80**, 155457 (2009).
41. Banerjee, D. et al. Convenient and mild epoxidation of alkenes using heterogeneous cobalt oxide catalysts. *Angew. Chem. Int. Ed. Engl.* **53**, 4359–4363 (2014).
42. Tian, S. et al. Carbon nitride supported Fe_2 cluster catalysts with superior performance for alkene epoxidation. *Nat. Commun.* **9**, 2353 (2018).
43. Im, J., Shin, H., Jang, H., Kim, H. & Choi, M. Maximizing the catalytic function of hydrogen spillover in platinum-encapsulated aluminosilicates with controlled nanostructures. *Nat. Commun.* **5**, 3370 (2014).
44. Wang, C. et al. Product selectivity controlled by nanoporous environments in zeolite crystals enveloping rhodium nanoparticle catalysts for CO_2 hydrogenation. *J. Am. Chem. Soc.* **141**, 8482–8488 (2019).
45. Nabaho, D., Niemantsverdriet, J. W., Claeys, M. & van Steen, E. Hydrogen spillover in the Fischer–Tropsch synthesis: an analysis of gold as a promoter for cobalt–alumina catalysts. *Catal. Today* **275**, 27–34 (2016).
46. Beaumont, S. K., Alayoglu, S., Specht, C., Kruse, N. & Somorjai, G. A. A nanoscale demonstration of hydrogen atom spillover and surface diffusion across silica using the kinetics of CO_2 methanation catalyzed on spatially separate Pt and Co nanoparticles. *Nano Lett.* **14**, 4792–4796 (2014).
47. Abbas, I., Kim, H., Shin, C. H., Yoon, S. & Jung, K.-D. Differences in bifunctionality of ZnO and ZrO₂ in Cu/ZnO/ZrO₂/Al₂O₃ catalysts in hydrogenation of carbon oxides for methanol synthesis. *Appl. Catal. B Environ.* **258**, 117971 (2019).
48. Spreafico, C., Karim, W., Ekinci, Y., van Bokhoven, J. A. & VandeVondele, J. Hydrogen adsorption on nanosized platinum and dynamics of spillover onto alumina and titania. *J. Phys. Chem. C* **121**, 17862–17872 (2017).
49. Choi, M., Yook, S. & Kim, H. Hydrogen spillover in encapsulated metal catalysts: new opportunities for designing advanced hydroprocessing catalysts. *ChemCatChem* **7**, 1048–1057 (2015).
50. Lu, J. et al. Coking-and sintering-resistant palladium catalysts achieved through atomic layer deposition. *Science* **335**, 1205–1208 (2012).
51. Marimuthu, A., Zhang, J. & Linic, S. Tuning selectivity in propylene epoxidation by plasmon mediated photo-switching of Cu oxidation state. *Science* **339**, 1590–1593 (2013).
52. Greiner, M. T., Jones, T. E., Klyushin, A., Knop-Gericke, A. & Schlögl, R. Ethylene epoxidation at the phase transition of copper oxides. *J. Am. Chem. Soc.* **139**, 11825–11832 (2017).
53. Ozbek, M. O. & van Santen, R. A. The mechanism of ethylene epoxidation catalysis. *Catal. Lett.* **143**, 131–141 (2013).
54. Kokalj, A., Gava, P., De Gironcoli, S. & Baroni, S. What determines the catalyst’s selectivity in the ethylene epoxidation reaction. *J. Catal.* **254**, 304–309 (2008).
55. Li, G., Wang, B. & Resasco, D. E. Water-mediated heterogeneously catalyzed reactions. *ACS Catal.* **10**, 1294–1309 (2020).
56. Rawat, K. S., Mahata, A. & Pathak, B. Thermochemical and electrochemical CO_2 reduction on octahedral Cu nanocluster: role of solvent towards product selectivity. *J. Catal.* **349**, 118–127 (2017).
57. Merte, L. R. et al. Water-mediated proton hopping on an iron oxide surface. *Science* **336**, 889–893 (2012).

Acknowledgements

We acknowledge the financial support from the National Natural Science Foundation of China (21773282, U1932131, U1832208, and 21673269), National Science Fund for Distinguished Young Scholars (21825204), the National Key R&D Program of China (2017YFA0700101), Natural Science Foundation of Shanxi Province (201801D211011), Excellent Youth Scholars of State Key Laboratory of Coal Conversion (2016BWZ004), and Youth Innovation Promotion Association of the Chinese Academy of Sciences (2018208). We are grateful to all staff at the 1W1B beamline of the Beijing Synchrotron Radiation Facility, Institute of High Energy Physics, Chinese Academy of Sciences, and at BL14W1 beamline of the Shanghai Synchrotron Radiation Facility, Shanghai Institute of Applied Physics, Chinese Academy of Sciences.

Author contributions

Z.G. and Y.Q. conceived the idea and supervised the work. M.X. synthesized the catalysts and performed the activity tests. G.W., J.Y.M., and Z.J. helped to perform or provide the XAFS measurement. S.X., W.Y., and P.W. assisted in the synthesis and characterizations of the catalysts. P.Z., X.L., J.P.M., and J.X. provided valuable suggestion for the improvement of the work. M.X., Z.G., and Y.Q. wrote the manuscript. All authors contributed to the manuscript.

Competing interests

The authors declare no competing interests.

Additional information

Supplementary information is available for this paper at <https://doi.org/10.1038/s41467-020-18567-6>.

Correspondence and requests for materials should be addressed to Z.G. or Y.Q.

Peer review information *Nature Communications* thanks Greiner and the other, anonymous, reviewer(s) for their contribution to the peer review of this work.

Reprints and permission information is available at <http://www.nature.com/reprints>

Publisher’s note Springer Nature remains neutral with regard to jurisdictional claims in published maps and institutional affiliations.



Open Access This article is licensed under a Creative Commons Attribution 4.0 International License, which permits use, sharing, adaptation, distribution and reproduction in any medium or format, as long as you give appropriate credit to the original author(s) and the source, provide a link to the Creative Commons license, and indicate if changes were made. The images or other third party material in this article are included in the article's Creative Commons license, unless indicated otherwise in a credit line to the material. If material is not included in the article's Creative Commons license and your intended use is not permitted by statutory regulation or exceeds the permitted use, you will need to obtain permission directly from the copyright holder. To view a copy of this license, visit <http://creativecommons.org/licenses/by/4.0/>.

© The Author(s) 2020